Length Scale Dependent Elasticity in Random Three-Dimensional Fiber Networks

Stephen Tyznik[1,2], Jacob Notbohm[1,2,*]

[1]Department of Engineering Physics

[2]Department of Mechanical Engineering

University of Wisconsin–Madison

Madison, WI, 53706

* Corresponding author:

Jacob Notbohm

University of Wisconsin–Madison

1500 Engineering Drive

Madison, WI, 53706

jknotbohm@wisc.edu

Abstract

The mechanics of fibrous materials are complicated by complex deformation mechanisms that result from the discrete fibrous structure. Though it is known that fibrous materials deform primarily by rotating and bending of fibers, the implications of rotating and bending on the mechanics of the network are not fully clear. Previous studies have investigated some effects of the fiber rotation and bending, observing fibers to rotate into directions of maximum principal stress, resulting in strain stiffening, and fibers under compression to buckle, resulting in compression softening. Nonlinear constitutive models have recently been developed to account for these deformation mechanisms, but the classical constitutive models that account for only stress and strain cannot fully account for fiber rotations and bending. Here, we interpret the mechanics of fibrous materials through

micropolar elasticity, also called Cosserat elasticity, which differs from classical elasticity in that it accounts for local moments caused by rotation of points within a material. The resulting equations can be written in terms of characteristic lengths that cause stress to depend on both strain and the length scale of the material. We simulated three-dimensional networks of fibers and observed a strong effect of length scale on the stiffness of networks in bending with a more mild effect in torsion. The length-scale dependence of stiffness is consistent with micropolar elasticity and can be described in terms of characteristic lengths of the material. Factors affecting the characteristic length were investigated by altering the fiber density, alignment, and bending stiffness. Although density was found to have no effect on characteristic length, increased fiber alignment led to a decrease in characteristic length, and increased fiber bending stiffness led to an increase in characteristic length. These findings suggest that the characteristic length is increased by factors that increase bending moments supported by the fibers. Although our parameter study manipulated the magnitude of characteristic length, no combination of parameters gave a characteristic length of zero, indicating that the mechanics of fibrous materials depend on length scale.

Key words

Fiber network, micropolar, Cosserat, characteristic length, length-scale dependence

1 Introduction

The shape and stiffness of many biological materials result from an underlying network of structural fibers. Such materials have complex mechanics. Fibers under tension reorient and align, causing the fiber network to strain stiffen (Onck et al., 2005; Vader et al., 2009; Stein et al., 2011; Münster et al., 2013; Rudnicki et al., 2013; Aghvami et al., 2016). Fiber alignment can also turn a nominally isotropic network into an anisotropic one, leading to interesting observations such as an apparent Poisson's ratio that exceeds the isotropic limit of 0.5 (Roeder et al., 2009; Vader et al.,

2009). Under compressive stress, fibers buckle (Münster et al., 2013; Kim et al., 2014; Burkel & Notbohm, 2017), which reduces the stiffness in compression (van Oosten et al., 2016). The loss of resistance to compression causes densification of compressed fibers, which creates a transition to a new, densified phase, similar to observations in foams (Kim et al., 2016; Liang et al., 2017).

The mechanics become more complex at smaller length scales, *e.g.*, tens of microns, which matches the size of a biological cell. At this scale, cell-induced forces can locally provoke the phase transition, causing dense bands of fibers that propagate from one cell to the next (Stopak & Harris, 1982; Korff & Augustin, 1999; Sawhney & Howard, 2002; Vader et al., 2009; Notbohm et al., 2015; Sopher et al., 2018; Grekas et al., 2019). In addition, fiber buckling causes local displacements, like those induced by a cell, to propagate over a longer range than predicted by classical linear elasticity (Winer et al., 2009; Rudnicki et al., 2013; Notbohm et al., 2015; Rosakis et al., 2015; Burkel & Notbohm, 2017; Grimmer & Notbohm, 2018). The fibrous structure also produces heterogeneity in the stress and displacement fields at scales on the order of 10–50 μm (Arevalo et al., 2015; Wen et al., 2007; Burkel et al., 2018). These heterogeneities result from heterogeneity in the local stiffness of the fiber network (Velegol & Lanni, 2001; Kotlarchyk et al., 2011; Shayegan & Forde, 2013; Jones et al., 2015; Proestaki et al., 2019). Another complication caused by the fibrous structure is that fibers can change both position (by translating) and angle (by bending/twisting). Classical theories of elasticity, both linear and nonlinear, consider points in space to only translate, not rotate. In classical theories, changes in angle result from the collective action of multiple points. This may be a limitation for fibrous materials, as a single point on a fiber could change both position and angle. Therefore, interpreting the mechanics of fibrous materials through classical elasticity may limit understanding.

The theory of micropolar elasticity, also called Cosserat elasticity, may be more accurate for fibrous materials as it takes into account local rotations and moment transfer within a material. In micropolar elasticity, there exists both a stress tensor $\boldsymbol{\sigma}$ (having units of force per area) and a couple stress tensor $\boldsymbol{m}$ (having units of torque per area). These are related to the strain tensor

$\boldsymbol{\varepsilon}$ and a vector defining the microrotation of individual points $\boldsymbol{\phi}$. The full constitutive relation is given by Eringen (1968):

$$\sigma_{ij} = \lambda\varepsilon_{kk}\delta_{ij} + 2G\varepsilon_{ij} + \kappa_m e_{ijk}(r_k - \phi_k), \tag{1}$$

$$m_{ij} = \alpha\frac{\partial\phi_k}{\partial x_k}\delta_{ij} + \beta\frac{\partial\phi_i}{\partial x_j} + \gamma\frac{\partial\phi_j}{\partial x_i}, \tag{2}$$

where δ_{ij} is the Kronecker delta, e_{ijk} is the permutation symbol, and summation over repeated indices is implied. The constants G and λ are the shear and Lamé moduli, having the same meaning as in classical elasticity (Lakes, 2016). Vector $\boldsymbol{r}$ is a macroscale rotation given by $r_i = (1/2)e_{ijk}\partial u_k/\partial x_j$ where $\boldsymbol{u}$ is the displacement vector. Of the remaining constants, α, β, and γ are micropolar terms that define the sensitivity of the material to rotation gradients, and have units of torque per distance. κ_m relates the micro and macro rotation fields and has units of force per area. These constants can be rearranged to define inherent length scales of a micropolar material. For example the characteristic lengths in bending, l_b, and torsion, l_t, are given by the following (Gauthier & Jahsman, 1975):

$$l_b = \sqrt{\frac{\gamma}{4G}}, \tag{3}$$

$$l_t = \sqrt{\frac{\beta+\gamma}{2G}}. \tag{4}$$

Energy considerations impose limits on these constants (Gauthier & Jahsman, 1975). Notably, $-1 < \beta/\gamma < 1$, and therefore $0 < l_t < 2l_b$, meaning that the characteristic length in torsion is bounded to being no more than twice the characteristic length in bending. However, l_b can be infinitely larger than l_t.

At length scales within an order of magnitude of l_b and l_t, micropolar elasticity predicts deviations from classical elasticity. For example, beams made of micropolar material with diameters on the order of l_b and l_t have greater stiffness in torsion and bending than predicted by classical elasticity. For beams with substantially larger diameters, the length-scale effect becomes unimportant and the stiffness of classical elasticity is recovered (Gauthier & Jahsman, 1975; Reddy & Venkata-

subramanian, 1978; Rueger & Lakes, 2016a). Micropolar materials also exhibit stress reduction in the vicinity of circular holes under tension, with the effect increasing as hole size decreases (Kulesh et al., 2001). The effects of micropolar theory in materials with cracks depend on the crack size and shape. For the simple case of a center crack in an infinite plate under mode I loading, the stress intensity factor depends on crack length: for crack lengths smaller (greater) than the micropolar characteristic length, the stress intensity factor is smaller (greater) than predicted by classical linear elasticity (Li & Lee, 2009).

Characteristic lengths associated with micropolar theory are typically related to an inherent length within the material. For example, in foams, the characteristic length is on the order of size of the foam's ribs (Rueger & Lakes, 2016a). As fibers provide structure in a similar way to ribs of a foam, it is reasonable to hypothesize that fibrous materials exhibit a characteristic length described by micropolar theory. Previous research testing this hypothesis remains limited. There is evidence that fibrous networks can be described by couple stress elasticity, a special case of micropolar elasticity (Reda et al., 2018; Berkache et al., 2019b). However, studies have observed other effects of length scale, such as modulus depending on network size (Shahsavari & Picu, 2013) and mechanics consistent with strain gradient elasticity (Reda et al., 2018; Berkache et al., 2019a), which are described by theories other than micropolar elasticity.

In this work, we studied the effect of length scale as described by the characteristic lengths in micropolar elasticity. Using a three-dimensional (3D) fiber network model, cylinders of different radii were loaded under torsion and bending boundary conditions. The stiffnesses in torsion and bending were compared to classical elasticity, and the data were used to compute the characteristic lengths. We then investigated the effects of fiber density, alignment, and bending stiffness on the characteristic lengths.

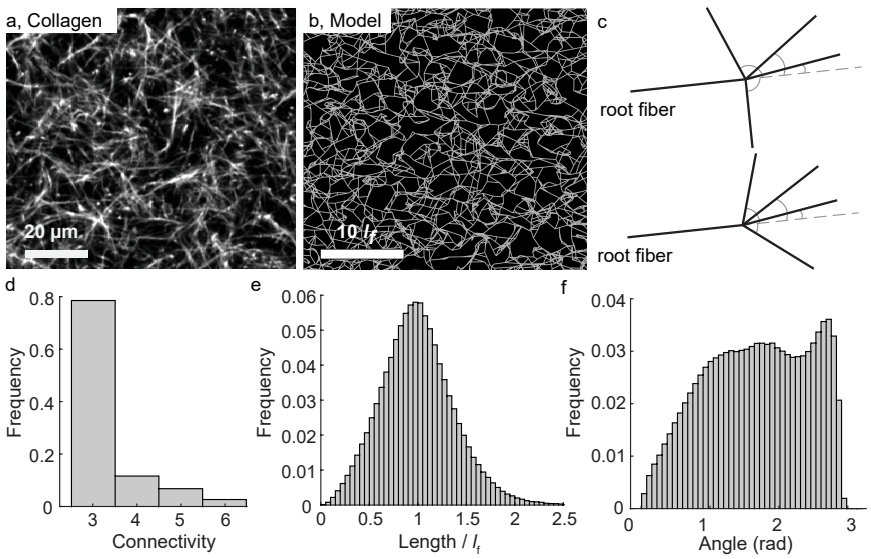

Figure 1: (a) Structure of a typical gel made of collagen I fibers. (b) Sample fiber network structure used to model gels of collagen I. (c) Sketch showing branching procedure described in the Methods section. The top sketch shows fibers (black) connected to a node before the branching procedure with the branch angles labeled in gray. The bottom sketch shows the fibers after the branching procedure; notice angles are reduced. (d–f) Histograms of connectivity (d), fiber length normalized by the mean fiber length l_f (e) and angles between all connecting fibers (f) for a representative simulated network.

2 Methods

2.1 Network Generation

To generate the random fiber networks, we used a method described by Grimmer & Notbohm (2018), which is based on a network generation method by Lindström et al. (2010, 2013). This method was designed to generate 3D networks of fibers that match those of extracellular matrix materials like collagen (Fig. 1a–b), and we refer to it as the simulated annealing method. Nodes, which later became fiber endpoints, were placed randomly within a cylindrical domain until a desired nodal density per unit volume was achieved. Nodal connectivity, the number of fibers that used a given node as an endpoint, was then randomly assigned for each node in the range of 2–6 such that the average value was 3.4. Fibers were then connected to nodes randomly until at least 98% of the nodal connectivities were satisfied. Next, a penalty function, defined as the sum of squares of the differences between the current fiber lengths and a desired fiber length,

was introduced. Nodes were sequentially modified either by swapping fibers with a nearby node or by a random translation. Both of these modifications occurred with equal probability. If the modification reduced the penalty function, it was accepted. If the modification caused the penalty function associated with the fibers connected to the modified nodes to increase by less than 20%, it was accepted with a 5% chance. All other modifications were rejected. Iterations were repeated until the penalty function reached 0.5% of its initial value.

Connections between fibers typically branch, with many acute angles between the fibers (Fig. 1a, c) (Rens et al., 2016; Grimmer & Notbohm, 2018). To mimic fiber branching, we used another penalty function, referred to as the branching penalty function. For each node, we identified the two fibers at that node that were most closely aligned. Of those two fibers, the one that was least aligned with the others was defined as the "root fiber"; branch angles were defined to be the angles supplementary to the angles formed between each fiber and the root fiber (Fig. 1c). A local penalty function was defined as the sum of the branch angles at each node; the branching penalty function was then the sum over all nodes. Once again nodes were moved to change the angles of all fibers other than the root fiber. Changes that reduced the branching penalty function were accepted. Additionally, changes that increased the local penalty function by 20% were accepted with a probability of 1%. As above, the procedure was carried out sequentially on each node, and iterations were repeated until the total branching penalty function became $< 30\%$ if its initial value. Histograms showing distributions of connectivity, fiber length, and all angles between connecting fibers are shown for a representative network in Fig. 1d–f.

2.2 Fiber Density

We defined fiber density as the number of fibers N_f divided by the unitless volume of the cylindrical domain,

$$n = \frac{N_f}{V/l_f^3}, \tag{5}$$

where the average fiber length l_f sets the length scale, so unitless volume is the cylinder volume V divided by l_f^3. Our method of network generation allowed for controlling the number of fibers N_f separately from average fiber length l_f. However, the simulated annealing method altered fiber lengths, which prohibited precise control of average fiber length, making it impossible to precisely control the density n. Therefore, networks having density in a prescribed range were used. Except where stated in the text, the range used was $1 \leq n \leq 1.4$.

2.3 Fiber Alignment

In some simulations, fibers were aligned along a preferred direction. To produce alignment, the positions of the nodes were adjusted. First, the center of the network was determined and nodes were translated outward from the center along the preferred direction of alignment. Secondly, the nodes were translated inwards in the off-axis directions by an amount that conserved the volume of the network. Lastly, all nodes were moved inward such that the average fiber length matched the initial fiber length. For all nodal adjustments, the magnitude of the translation was proportional to the initial distance from each node to the center of the network.

To quantify fiber alignment, the 3D order parameter S was used:

$$S = \frac{1}{2} \left\langle 3 \cos^2 \theta_i - 1 \right\rangle, \tag{6}$$

where subscript i indicates the i-th fiber, and the brackets $<>$ indicate a mean over all fibers. The angle θ_i is the angle between the fiber's orientation and the preferred direction of alignment which was defined as axially along the cylinder. S takes a value of 0 when fibers orientations are random and a value of 1 when all fibers are aligned with the cylinder's axis. Alignment was studied in only one set of simulations as described in the text; no fiber alignment (*i.e.*, $S \approx 0$) was present in the other simulations.

2.4 Fiber Mechanical Properties

Fibers in the network were modeled as Timoshenko beams having bending stiffness k_b, axial stiffness k_a, and shearing stiffness k_s. The two stiffnesses can be combined into two dimensionless ratios. The most important ratio is that between the bending and axial stiffnesses, $\kappa = k_b/k_a = (E_f I_f)/(E_f A_f l_f^2)$, where E_f is the fiber's Young's modulus, A_f is its cross sectional area, and I_f is its moment of inertia. Assuming each fiber has circular cross section of radius r_f, the dimensionless stiffness κ is proportional to r_f^2/l_f^2. As pointed out previously (Licup et al., 2015; Vahabi et al., 2016; van Oosten et al., 2016), the ratio r_f^2/l_f^2 is also proportional to the volume fraction of fibers as follows: volume fraction is given by fiber volume over total volume, i.e., volume fraction equals $\pi r_f^2 l_f/l_f^3$, which is proportional to r_f^2/l_f^2. Hence, κ is proportional to the volume fraction of the fiber network, which is in the range of $10^{-4} - 10^{-2}$ (Licup et al., 2015; Vahabi et al., 2016; van Oosten et al., 2016). It is common for theoretical models to test a larger range of κ, *e.g.*, $10^{-7} - 10^{0}$, which accounts for networks dominated by bending (low κ) and stretching (high κ) (Wilhelm & Frey, 2003; Head et al., 2003; Onck et al., 2005; Hatami-Marbini & Picu, 2008; Conti & MacKintosh, 2009; Broedersz et al., 2011). Except where stated in the text, we used a value of $\kappa = 10^{-4}$, as this value is typical of fibrous gels made of collagen. A second ratio defines the dimensionless ratio between shearing and axial stiffnesses of each fiber, $\kappa_s = k_s/k_a = G_f/E_f$, where G_f is the fiber's shear modulus. Except where stated in the text, all simulations used a value of $\kappa_s = 1/2$.

2.5 Geometry and Boundary Conditions

Cylinders of different radii were simulated. To produce the different cylinders, each fiber network having starting radius of $R/l_f = 65$ was cut multiple times to generate multiple cylinders of smaller radii in the range of $6 \leq R/l_f \leq 65$. Cutting was performed by removing fibers that were entirely outside the desired cylinder volume. Rather than remove fibers that intersected the boundary, the nodes outside were translated to be exactly on the boundary to reduce heterogeneity along the boundaries. The cylinders were then subjected to torsion, bending, and uniaxial extension.

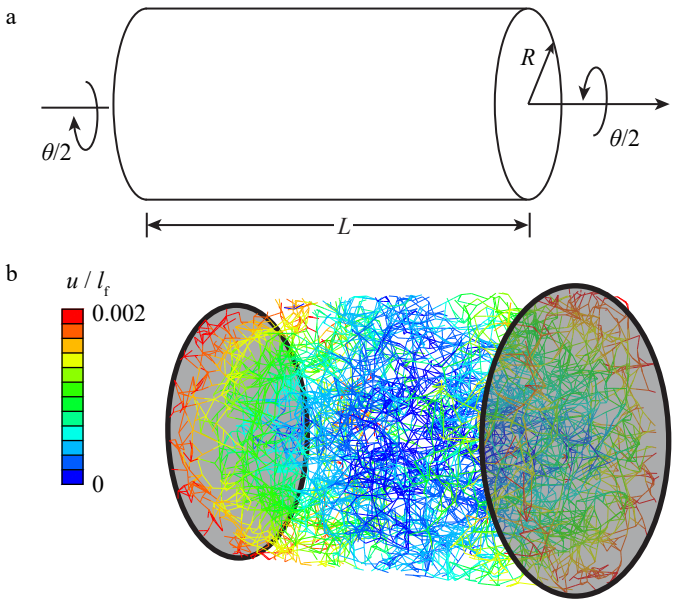

Figure 2: (a) Boundary conditions applied in torsion induced a rotation of $\theta/2$ on each end of the cylinder, giving a relative rotation angle of θ. (b) Representative fiber network having radius of $10l_f$ and length of $30l_f$ under torsion. Gray circles show ends where boundary conditions were applied. Color shows magnitude of displacement u/l_f.

For torsion simulations, a rotation of $\theta/2$ was applied to each boundary for a relative rotation of θ as shown in Fig. 2. Cylinder length L and applied rotation $\theta = 0.001$ rad were the same for all torsion simulations. For bending, a rotation of ψ was applied to each boundary of the cylinder for a total rotation of 2ψ as shown in Fig. 3a–c. The resulting radius of curvature was $\rho = L/(2\psi)$. A dimensionless value of $\rho/l_f = 865$ was used for all bending simulations. For the networks having largest radius, $R/l_f = 65$, this radius of curvature produced a maximum network-level strain of 13%. Deformations of individual remained small, as shown by histograms of fiber axial strain, rotation angle, and curvature for a representative network having a radius $R/l_f = 65$ (Fig. 3d–f).

The 3D beams used had six degrees of freedom, three for translation in the X, Y, and Z directions and three for rotation about those axes. For both torsion and bending simulations, the translational and rotational degrees of freedom were prescribed on the left and right faces of each cylinder, as illustrated in Fig. 3b. The nodal rotation was equal to the rotation of the cylinder face.

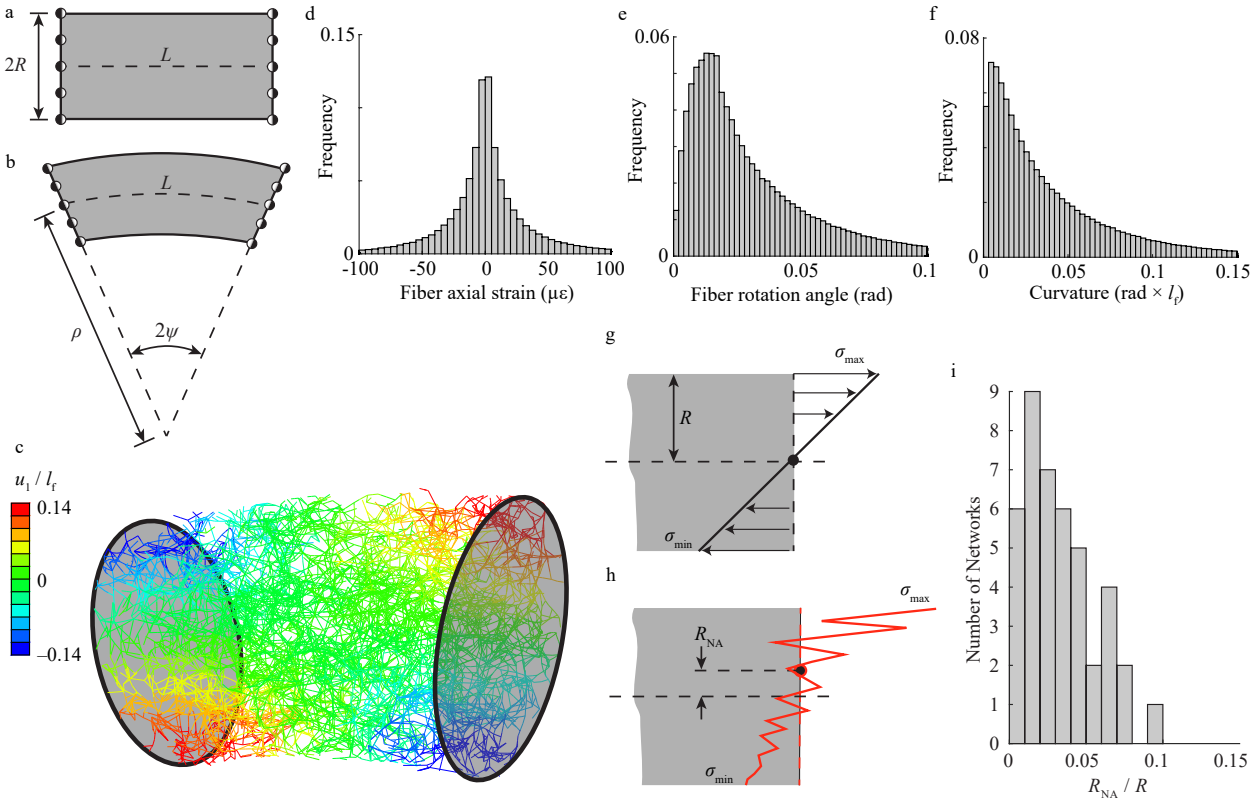

Figure 3: (a) Planar view of 3D cylinder geometry, with radius R and length L. (b) Deformed geometry of the cylinder under pure bending boundary conditions. Nodes on cylinder faces were displaced and rotated such that $L = 2\psi\rho$. (c) Representative fiber network having radius $10l_f$ and length $30l_f$ under bending. Gray circles show faces where boundary conditions were applied. Color shows the component of displacement along the axis of the cylinder. (d–f) Histograms showing distributions of axial strain (d), rotation angle (e), and dimensionless curvature (f) for each fiber of a single representative network of radius $R/l_f = 65$ in bending. (g) Distribution of stresses in a classically linear elastic material under bending. The neutral axis is located at the center of cylinder. (h) Example of the distribution of stresses due to bending of a heterogeneous material similar to the fiber networks studied here. Due to heterogeneity, the neutral axis is not necessarily located at the center of the cylinder. (i) Histogram of normalized distance from center of cylinder to neutral axis, R_{NA}/R for multiple fiber networks tested under bending.

2.6 Finite Element Solver

The finite element software Abaqus 6.16 (Dassault Systèmes) was used to compute the forces and moments resulting from the prescribed boundary conditions. Fibers were modeled as 3D, 3-node, quadratic, Timoshenko beam elements. Connections between fibers were made by tying FE nodes together, which transmitted both forces and moments between fibers. Deformations were induced using displacement and rotation boundary conditions. Applied deformations were sufficiently small

such that the maximum strain based on predictions of continuum mechanics remained below 1%. The implicit static solver with the nonlinear geometry option was used for all computations. In comparison to the implicit dynamic quasi-static solver, the static solver produced nearly identical results with a much lower computational time.

The forces and moments within each fiber were output from the finite element software and used for later analysis. In the uniaxial extension simulations, the total force supported by each network was computed from the reaction forces at the boundaries. In the torsion and bending simulations, the total moment was computed by taking the cross product between the position and reaction force of each node on the cylinder boundaries. To compute each node's position, the origin was taken as the center of the face corresponding to that node. In bending, this computation assumed that the neutral axis remained at the center of the cylinder, which is true for a homogeneous, linear, elastic material (Fig. 3g) but may not be true for a heterogeneous material (Fig. 3h). To verify this assumption, we fit a line to axial force versus distance from the center of the cylinder and computed the intercept, which gave the distance to the neutral axis R_{NA}. Repeating this procedure for many different cylinders produced a histogram. Nearly all values of normalized distance to the neutral axis R_{NA}/R were < 0.1 with most values < 0.05 (Fig. 3i). These small values indicate that the assumption of the neutral axis being located at the center of the cylinder produced minimal error.

3 Analysis

Young's modulus and Poisson's ratio for each network were computed using simulations in uniaxial extension. The Young's modulus of each fiber network E_n was computed from the applied force F, the cross sectional area A, and the axial strain ε according to the equation $E_n = F/(A\varepsilon)$.A previous study observed Young's modulus to depend on the size of a fiber network (Shahsavari & Picu, 2013). The networks used in our study showed a similar dependence on size with dimensionless network modulus E_n/E_f decreasing in networks having small radius (Fig. 4). Although this observation is inconsistent with micropolar elasticity, it does not rule out the possibility that

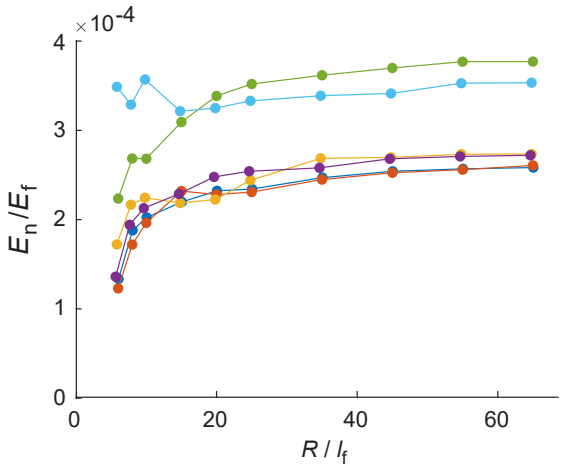

Figure 4: Dimensionless Young's modulus of cylinders of random fiber networks subjected to uniaxial tension. Each color corresponds to one random network, and the points represent cylinders of different radii cut from that network. Network properties used were $\kappa = 10^{-4}$, $\kappa_s = 1/2$, $S = 0$, and $1 \leq n \leq 1.4$.

micropolar elasticity describes effects of length scale in torsion and bending. To avoid artifacts in our analysis caused by the dependence of Young's modulus on cylinder radius, we analyzed the results using two different definitions of Young's modulus for each cylinder. The first defined Young's modulus to be the value computed for the largest dimensionless radius of $R/l_f = 65$; the second defined Young's modulus to be the value computed for each radius. Most figures in this manuscript compare results obtained with both definitions.

The Poisson's ratio of each network ν was computed from the ratio of macroscale normal strains, which were computed by fitting lines to nodal displacements against nodal position and taking the slopes. As the resulting values of Poisson's ratio were heterogeneous with a mean of 0.25 and a standard deviation of 0.07, the mean value was used for all networks rather than their individually computed values.

Torsion and bending were simulated to compute apparent moduli under these boundary conditions. For torsion, the apparent modulus is a function of ν, L, θ, the applied moment M, and the polar moment of inertia J:

$$E_t = 2(1+\nu)\frac{ML}{J\theta}. \tag{7}$$

If effects of length scale are present in torsion, the apparent modulus E_t differs from the actual modulus E_n. The ratio of E_t to E_n is a relative stiffness in torsion, which is computed according to the equation

$$\Omega_t = \frac{E_t}{E_n} = \frac{2(1+\nu)}{E_n}\frac{ML}{J\theta}. \tag{8}$$

The physical meaning of Ω_t is that it describes an increase in torsional stiffness as compared to predictions of classical linear elasticity. For classical elasticity, the relative stiffness Ω_t is equal to 1, whereas in micropolar elasticity it has values in the range $1 < \Omega_t < \infty$ (Gauthier & Jahsman, 1975). The relative stiffness in torsion of micropolar cylinders has the approximate form (Rueger & Lakes, 2016a)

$$\Omega_t \approx 1 + 6\left(\frac{l_t}{R}\right)^2, \tag{9}$$

where l_t is the characteristic length in torsion (Eq. 4).

The same comparison to classical elasticity can be made for a material under pure bending. Here the apparent modulus depends on the applied moment M the radius of curvature of the deformed cylinder ρ and the moment of inertia of the network's cross section I_n.

$$E_b = \frac{M\rho}{I_n} \tag{10}$$

Again, the apparent modulus may differ from the Young's modulus, because micropolar theory predicts a length-scale effect for bending of cylinders. The relative stiffness in bending, Ω_b, is given by

$$\Omega_b = \frac{E_b}{E_n} = \frac{M\rho}{I_n E_n}. \tag{11}$$

The effect of length scale on relative stiffness is predicted by micropolar theory and has the approximate form (Rueger & Lakes, 2016a)

$$\Omega_b \approx 1 + 8\left(\frac{l_b}{R}\right)^2 \frac{1-(\beta/\gamma)^2}{1+\nu}, \tag{12}$$

where l_b is the characteristic length in bending (Eq. 3) and β and γ are the material constants in Eq. 2.

In this study, variables having units of length were made dimensionless by dividing by the average fiber length l_f. Eqs. 9 and 12 can therefore be rewritten as

$$\Omega_t \approx 1 + 6\left(\frac{l_t/l_f}{R/l_f}\right)^2 \tag{13}$$

and

$$\Omega_b \approx 1 + 8\left(\frac{l_b/l_f}{R/l_f}\right)^2 \frac{1-(\beta/\gamma)^2}{1+\nu}. \tag{14}$$

These equations allowed for computing the dimensionless characteristic lengths in torsion and bending l_t/l_f and l_b/l_f by fitting the relative stiffnesses Ω_t and Ω_b against dimensionless cylinder radius R/l_f.

4 Results

To study the effects of length scale in torsion, we simulated cylinders of fibers under torsion and quantified the relative stiffness Ω_t according to Eq. 8. Simulations were done on six randomly generated networks, with each network cut to different cylinder radii in the range of $10l_f$ to $65l_f$. The simulations resulted in six data sets showing the effect of cylinder radius on relative stiffness. The data show a relative stiffness > 1 in cylinders with small radii (Fig. 5), which is inconsistent with classical elasticity but agrees with micropolar theory. The relative stiffness Ω_t has high heterogeneity at the smaller radii. Nevertheless, we fit the data to the micropolar approximation of relative stiffness of a cylinder under torsion (Eq. 13) using a nonlinear least square fitting. The curve fitting resulted in normalized characteristic lengths in the range $0.5 \leq l_t/l_f \leq 5.4$, with an average value of 3.0.

Thermodynamic considerations of the micropolar constants give limits on characteristic length

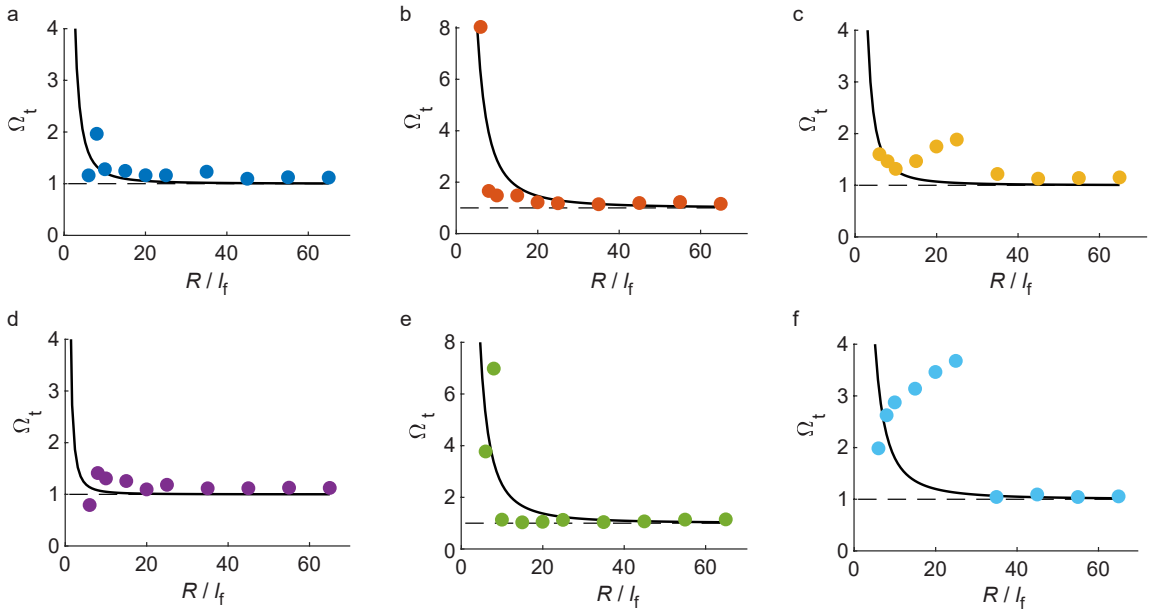

Figure 5: Relative stiffness of cylinders of random fiber networks subjected to torsion. Each plot corresponds to one random network, and the points represent cylinders of different radii cut from that network. Network properties used were $\kappa = 10^{-4}$, $\kappa_s = 1/2$, $S = 0$, and $1 \leq n \leq 1.4$. The dashed lines show the relative stiffness for a classically linear elastic material, $\Omega_t = 1$. The solid lines show the fits of Eq. 13 to the data. Panels a–f have characteristic lengths in torsion, $l_t/l_f = 1.7$, 5.4, 1.9, 0.5, 4.8, and 3.5 respectively.

in torsion of $0 < l_t$ (Gauthier & Jahsman, 1975). As it is possible that the characteristic length in torsion is very small, it may be that a clear length-scale effect in torsion would require fiber networks having such small radii that heterogeneity of the network dominates over effects of length scale. This could explain the large heterogeneity observed in Fig. 5. In considering both torsion and bending, characteristic lengths must satisfy to relationship $0 < l_t < 2l_b$ (Gauthier & Jahsman, 1975), which implies that even if the characteristic length in torsion is small, the characteristic length in bending may be large.

We therefore performed simulations in pure bending on the same fiber networks to quantify the relative stiffness in bending. The effect of network radius on relative stiffness was much stronger in bending as compared to torsion, with relative stiffnesses for networks having the smallest radii typically reaching values greater than 5 (Fig. 6). In this figure, the main plots show relative stiffness Ω_b as defined in Eq. 11 calculated by taking Young's modulus to be the value computed for the largest cylinder radius of $R/l_f = 65$; insets show Ω_b calculated using Young's modulus computed

for each cylinder radius. Comparison of each plot to the corresponding inset shows only modest differences, indicating that the increase in relative stiffness was insensitive to the effect of length scale on Young's modulus shown in Fig. 4. The increase in relative stiffness at small radii was also insensitive to the precise boundary conditions used, as other simulations of bending in a cylindrical network loaded by a point force at its tip produced similar values of relative stiffness as those shown in Fig. 6. In this manuscript, we show results only for pure bending, as there exists a theoretical solution of micropolar theory for pure bending (Reddy & Venkatasubramanian, 1978). The relative stiffnesses Ω_b for all radii and all networks closely matched the approximation to micropolar theory given by Eq. 14. Fits of the main plots in Fig. 6 to the theory (Eq. 14) gave characteristic lengths in bending in the range $5.1 \leq l_b/l_f \leq 6.6$ with an average value of 5.8. Fits to the insets gave slightly larger characteristic lengths, in the range $5.4 \leq l_b/l_f \leq 9.0$. These results indicate a clear effect of length scale in bending.

Next we considered the effects of changing fiber structure and properties on the characteristic length. Because some simulations in torsion did not match predictions of micropolar theory (Fig. 5), but all simulations in bending did (Fig. 6), we chose to focus on the characteristic length in bending for the remainder of our study. We began by changing the dimensionless number density of fibers n (defined in Eq. 5) in the range of 1 to 3. As expected, increasing the fiber number density n linearly increased the dimensionless modulus of the network E_n/E_f (Fig. 7a). For each network, the characteristic length in bending l_b was computed by fitting to plots of Ω_b vs. R as in Fig. 6. Surprisingly, fiber density had no clear effect on the characteristic length in bending (Fig. 7b, c). As micropolar theory predicts characteristic lengths to result from internal couple moments supported in a material, a possible explanation for density having no effect on characteristic length is that it does not affect the overall balance of moment and force in each fiber. To test this hypothesis, we analyzed the 3D internal forces F and moments M supported by each fiber by combining them into the dimensionless number

$$\Gamma = \frac{1}{2}\left\langle 1 + \frac{|M^i| - |F^i| l_f^i}{|M^i| + |F^i| l_f^i} \right\rangle, \tag{15}$$

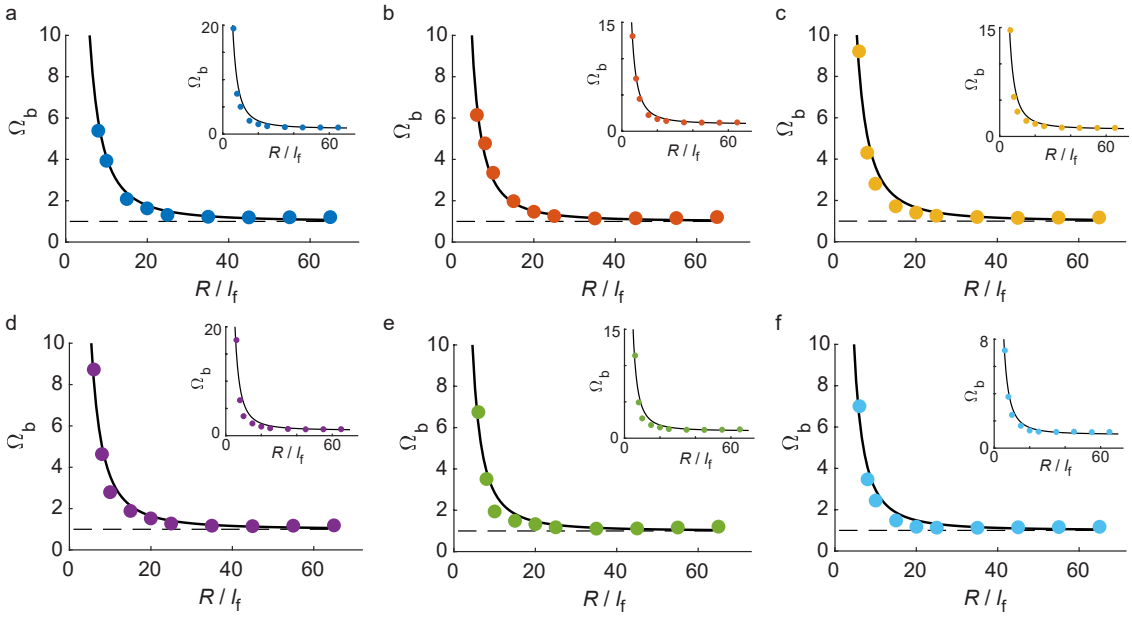

Figure 6: Relative stiffness of cylinders of random fiber networks under pure bending. Each plot corresponds to one random network, and the points represent cylinders of different radii cut from that network. Network properties used were $\kappa = 10^{-4}$, $\kappa_s = 1/2$, $S = 0$, and $1 \leq n \leq 1.4$. The dashed lines show the relative stiffness for a classically linear elastic material, $\Omega_b = 1$. The solid lines are fits of Eq. 14 to the data. Panels a–f have characteristic lengths in bending $l_b/l_f = 6.6$, 5.4, 6.1, 6.0, 5.1, and 5.2, respectively. Networks tested are identical to those shown in Fig. 5. Main figures show relative stiffness computed using the value of Young's modulus E_f corresponding to the largest radius, $R/l_f = 65$; insets show relative stiffness computed using the value of Young's modulus corresponding to each cylinder's radius.

where superscript i indicates the i-th fiber, and the brackets $<>$ indicate a mean over all fibers. Γ is bounded by $0 \leq \Gamma \leq 1$, where $\Gamma = 0$ indicates fibers in the network support only internal forces and $\Gamma = 1$ indicates fibers support only moments. Γ was found to be independent of fiber number density n (Fig. 7d), suggesting no effect of density on the balance of forces and moments within each fiber.

The variable Γ depends on the discrete moments and forces within each fiber, whereas micropolar theory assumes the material is not discrete but rather a continuum. We therefore defined a second dimensionless number Λ that still used the moment within each fiber but compared it to the magnitude of force in each fiber predicted by classical linear elasticity. To compute the force in each fiber predicted by classical linear elasticity, we began with the stress $|\sigma^i| = E_n y^i/\rho$, where y^i is the distance between the i-th fiber and the neutral axis. As the continuum stress is supported

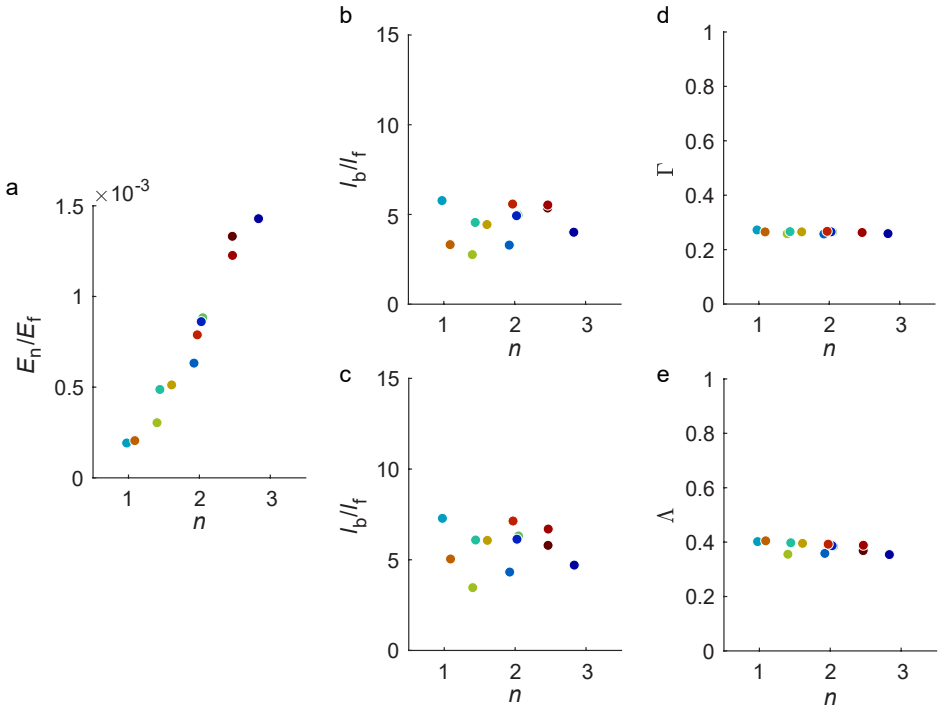

Figure 7: Effects of dimensionless fiber density n on (a) the dimensionless network uniaxial modulus E_n/E_f, (b, c) the normalized characteristic length in bending l_b/l_f, (d) the dimensionless parameter Γ, and (e) the dimensionless parameter Λ. Points in panel b were computed using the value of Young's modulus corresponding to the largest radius $R/l_f = 65$; points in panel c were computed using the value of Young's modulus corresponding to each cylinder's radius. Network properties used were $\kappa = 10^{-4}$, $\kappa_s = 1/2$, and $S = 0$. Each point is the value computed for one randomly generated network, cut to many different cylinder sizes. Each random network network is assigned a different color, which is used for all panels. Points in panels a, d, and e are averages over all cylinder sizes; points in panels b and c are from fits to Eq. 14.

by n fibers in a cross sectional area of l_f^2, the force supported by the i-th fiber is $|\sigma^i|l_f^2/n$. The dimensionless number Λ is therefore given by

$$\Lambda = \frac{1}{2}\left\langle 1 + \frac{|M^i| - \left(|\sigma^i|l_f^2/n\right) l_f^i}{|M^i| + \left(|\sigma^i|l_f^2/n\right) l_f^i} \right\rangle. \tag{16}$$

Again, $0 \leq \Lambda \leq 1$, where $\Lambda = 0$ indicates fibers in the network support no moments, and $\Lambda = 1$ indicates fibers support very large moments. The difference between Γ and Λ is that Γ considers local moments and forces in the fibers whereas Λ considers local moments in the fibers but forces predicted by continuum theory. Similar to its effect on Γ, fiber number density had negligible effect Λ (Fig. 7e). These findings are consistent with the notion that density had minimal effect

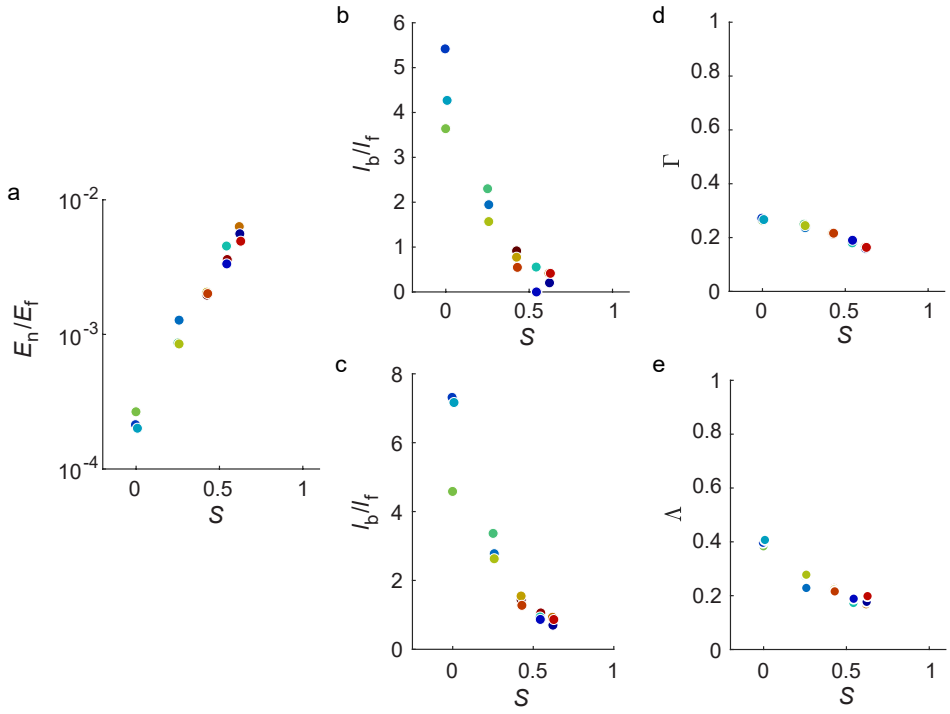

Figure 8: Effects of fiber alignment (quantified by order parameter S) on (a) the dimensionless network uniaxial modulus E_n/E_f, (b, c) the normalized characteristic length in bending l_b/l_f, (d) dimensionless parameter Γ, and (e) dimensionless parameter Λ. Points in panel b were computed using the value of Young's modulus corresponding to the largest radius $R/l_f = 65$; points in panel c were computed using the value of Young's modulus corresponding to each cylinder's radius. Network properties used were $\kappa = 10^{-4}$, $\kappa_s = 1/2$, and $1 \leq n \leq 1.4$. Each point is the value computed for one randomly generated network, cut to many different cylinder sizes. Each random network network is assigned a different color, which is used for all panels. Points in panels a, d, and e are averages over all cylinder sizes; points in panels b and c are from fits to Eq. 14.

on internal moments in the fibers and, therefore, minimal effect on the characteristic length in bending.

Next, the effect of fiber alignment was assessed by generating networks having different amounts of fiber alignment along the axis of the cylinder. As fibers aligned, the modulus in uniaxial tension increased (Fig. 8a). In bending, the characteristic length decreased with alignment (Fig. 8b, c), which may be the result of alignment causing fibers to support greater forces relative to moments. In agreement with this explanation, both Γ and Λ decreased with increasing alignment (Fig. 8d, e). Therefore, fiber alignment along the axis of the cylinder reduced the effect of length scale by reducing the relative magnitude of moments supported by each fiber.

Lastly, the dimensionless bending stiffness κ was considered by varying it over a range spanning a low, bending-dominated value of 10^{-6} to a large, stretching-dominated value of 10^{2}. The modulus in uniaxial extension increased with increasing bending stiffness until κ reached a value of $\sim 10^{-1}$ (Fig. 9a). For $\kappa \lesssim 10^{-1}$, the slope of the data matches the black line having a slope of 1 in Fig. 9a, which indicates modulus scales linearly with dimensionless bending stiffness κ in the bending-dominated regime, consistent with previous studies (Broedersz et al., 2011; Licup et al., 2016; Sharma et al., 2016; Rens et al., 2016). For $\kappa \gtrsim 10^{-1}$ there is a transition into a regime where normalized network modulus is insensitive to dimensionless bending stiffness κ. This new regime results from a transition from fiber bending to stretching (Head et al., 2003; Wilhelm & Frey, 2003; Conti & MacKintosh, 2009; Licup et al., 2016; Islam & Picu, 2018). Though the exact value of κ to cause the transition depends on the type of fiber network, a previous study observed the transition to occur near $\kappa = 2 \times 10^{-2}$ for cellular networks (Islam & Picu, 2018), which are similar in structure to the networks studied here. Networks were then subjected to bending to compute the characteristic lengths. We expected that increasing the dimensionless bending stiffness κ would affect the distribution of moments and forces in the fiber network. Consistent with our hypothesis, the characteristic length in bending increased with increasing values of κ above 10^{-1} (Fig. 9b, c). The critical value of $\sim 10^{-1}$ was the same whether the data were analyzed using the value of Young's modulus corresponding to the largest cylinder (Fig. 9b) or the value corresponding to each cylinder's radius (Fig. 9b). The dimensionless numbers Γ and Λ also increased with increasing κ (Fig. 9c, d). Notably, Γ and Λ each spanned a large range from 0.3 to 1, implying that the fibers transitioned from supporting primarily forces to supporting only moments as κ was increased. It is also noteworthy that E_n/E_f, Γ, and Λ all trend upward for $\kappa \gtrsim 10^{-1}$, which suggests that the transition of fiber bending to stretching caused an increase in characteristic length. Accordingly, the characteristic length increased with increasing κ for $\kappa \gtrsim 10^{-1}$.

The characteristic length also increased for small values of κ, with large values of characteristic length observed for the smallest value, $\kappa = 10^{-6}$. Though the cause of this increase is unknown, it may be related to the fact that heterogeneity, as quantified using different metrics for nonaffine

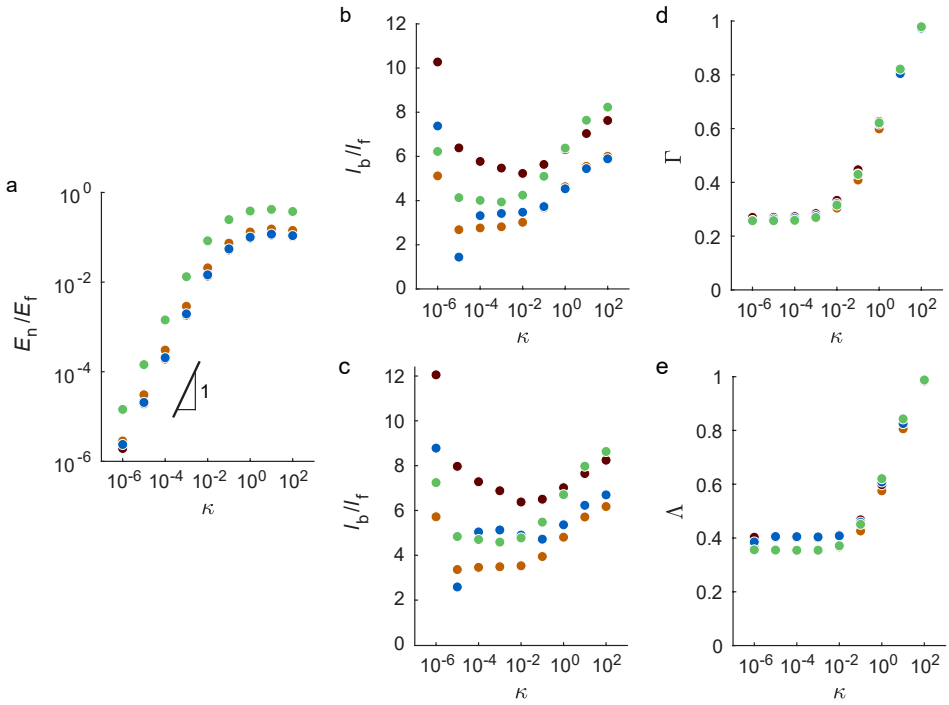

Figure 9: Effects of dimensionless bending stiffness, κ, on (a) the dimensionless network uniaxial modulus E_n/E_f, (b, c) the normalized characteristic length in bending l_b/l_f, (d) dimensionless parameter Γ, and (e) dimensionless parameter Λ. Points in panel b were computed using the value of Young's modulus corresponding to the largest radius $R/l_f = 65$; points in panel c were computed using the value of Young's modulus corresponding to each cylinder's radius. Each color represents results from one randomly generated network, cut to many different cylinder sizes. The four networks tested are chosen to be representative of the spectrum of random networks. The blue and green points represent networks having densities of $n = 1.09$ and $n = 2.83$ and characteristic lengths at $\kappa = 10^{-4}$ of $l_b/l_f = 5.0$ of $l_b/l_f = 4.7$, respectively. The orange and dark red points represent networks having densities of $n = 1.40$ and $n = 0.97$ but the maximum and minimum characteristic lengths at $\kappa = 10^{-4}$. All networks had $S = 0$. Points in panels a, d, and e are averages over all cylinder sizes; points in panels b and c are from fits to Eq. 14.

displacements, increased with decreasing bending stiffness κ (Head et al., 2003; Hatami-Marbini & Picu, 2008; Conti & MacKintosh, 2009). Consistent with this notion, we observed the relative stiffness in bending Ω_b to be highly heterogeneous for $\kappa = 10^{-6}$, with values of Ω_b ranging from 0.2 to 47. This heterogeneity in relative stiffness was present only for the smallest values of κ; for $\kappa \geq 10^{-4}$, heterogeneity in relative stiffness largely disappeared as demonstrated by Fig. 6.

Close inspection of Fig. 9a shows that at large values of dimensionless bending stiffness κ, the dimensionless network modulus E_n/E_f decreased. We suspected that the decrease resulted from the fact that the shear modulus of each fiber was of the same order of magnitude as the Young's

modulus, which could produce another deformation mechanism, fiber shearing, occurring for very large values of κ. We therefore increased the dimensionless fiber shear modulus κ_s by two orders of magnitude and repeated the simulations of Fig. 9. Under these conditions the network modulus increased monotonically with κ (Fig. 10a), confirming the predicted effect of fiber shearing. When the networks made of fibers with large shear modulus were subjected to bending, the general trends remained the same: l_b/l_f, Γ, and Λ all increased with increasing κ for $\kappa \gtrsim 10^{-1}$ (Fig. 10b–e). However, there were two notable differences. Firstly, the magnitude of characteristic length in bending l_b/l_f was larger for networks made of fibers with large shear modulus (Fig. 10b, c) compared to small shear modulus (Fig. 9b, c). Similarly, the magnitudes of Γ and Λ increased with increasing fiber shear modulus. This observation indicates that increasing the fiber shear modulus caused fibers to support greater bending moments. Secondly, comparison of Figs. 9b, c and 10b, c shows that increasing the fiber shear modulus reduced network-to-network heterogeneity in characteristic length for low values of κ. Fig. 10 therefore clarifies the effect of bending stiffness κ on characteristic length: it is relatively unaffected by κ for $\kappa \lesssim 10^{-1}$ and increases with κ above this value. Importantly, the fibers in real materials have a dimensionless shear modulus $\kappa_s \leq 1/2$, so the heterogeneity present in Fig. 9 is more representative of real materials than the data in Fig. 10.

5 Discussion

We investigated effects of micropolar elasticity in materials made of random fibers using a model designed to simulate biological materials such as gels of collagen fibers. The fibrous structure is similar to other materials shown to exhibit micropolar elasticity such as foams (Rueger & Lakes, 2016a) and bones (Yang & Lakes, 1981, 1982). We observed the stiffness to depend on length scale in bending with characteristic length found to be a few times larger than the average fiber length. To investigate factors affecting the characteristic length, we varied fiber density, alignment and bending stiffness. Density was found to have no effect on the characteristic length, whereas

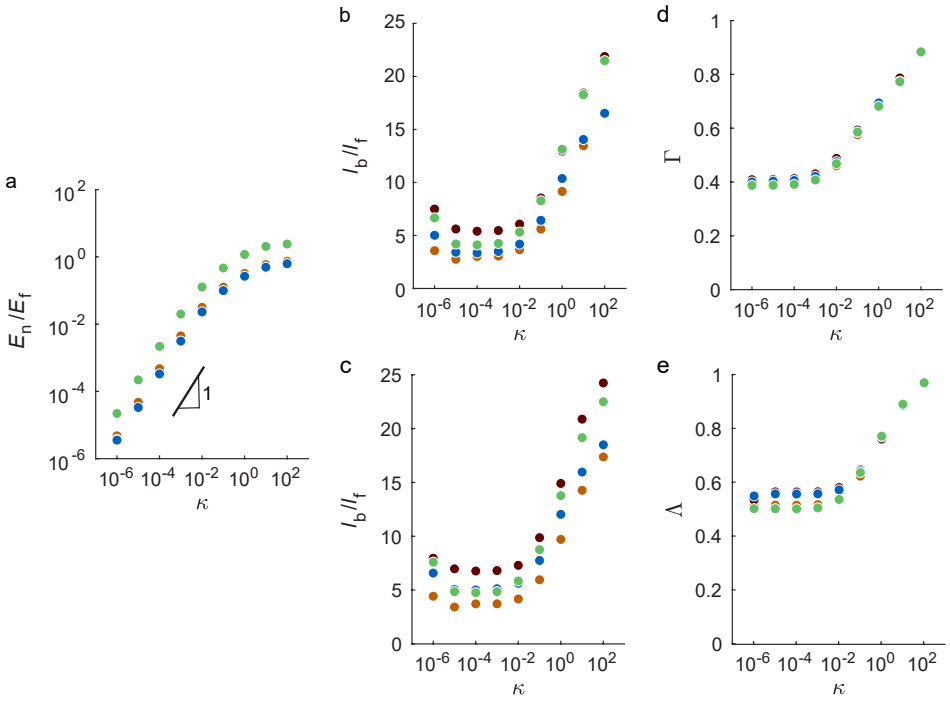

Figure 10: Effects of dimensionless bending stiffness, κ, with an increased shear modulus G on (a) the dimensionless network uniaxial modulus E_n/E_f, (b, c) the normalized characteristic length in bending l_b/l_f, (d) dimensionless parameter Γ, and (e) dimensionless parameter Λ. Plots are computed identically to Fig. 9. All networks had a large dimensionless shear modulus of $\kappa_s = 50$.

decreased alignment and increased bending stiffness each produced a greater characteristic length.

The observation that fiber density (number per unit volume) had no effect on the characteristic length (Fig. 7) differs from observations in other materials. In foams, the cell density (number of cells per unit volume) is coupled to cell size: increasing the number of cells per unit volume requires that the cell size be reduced, which in turn reduces the average lengths of the ribs. In turn, the reduced rib size reduces the characteristic length (Rueger & Lakes, 2016b). A similar case is present in bones and lattice structures. By contrast, the fiber networks studied here have no coupling between fiber density and fiber length. This feature is due to the fact that the long, thin fibers produce a network with a large amount of void space between them. As a result, fibers can be added to the network without connecting. The fact that density is unrelated to fiber length explains why density has no effect on characteristic length (Fig. 7). This observation is unique to the simulated annealing network generation method used here. Other methods of network generation,

such as those based on fiber growth, Voronoi tesselation, or lattices (Heussinger & Frey, 2007; Humphries et al., 2017) have a coupling between fiber length and fiber density and therefore may behave more like foams. This reasoning is supported by a previous study using networks based on the fiber growth method (Berkache et al., 2019b), which observed micropolar moduli to depend on the fiber density.

An increase in dimensionless fiber bending stiffness κ resulted in a greater characteristic length in bending l_b (Figs. 9–10), indicating a greater dependence on length scale. This observation is unintuitive, because greater bending stiffness produces deformations with less fiber bending and more fiber stretching. The transition from bending to stretching could be expected to reduce the microrotations associated with micropolar elasticity, but, in contrast, the data show an increase in characteristic length. It is important to note, however, that increasing the bending stiffness could affect both the microrotations and the micropolar elastic moduli that relate the microrotations to the couple stress. In this case, the increased characteristic length in bending l_b results from a change in the micropolar modulus γ and/or the shear modulus G as dictated by Eq. 3. The exact relationship between the bending stiffness and the micropolar elastic moduli is unclear, but it is reasonable to expect increasing bending stiffness κ to increase both the micropolar modulus γ and the shear modulus G. The increases in γ and G were not proportional, however, because the characteristic length in bending l_b was observed to increase. This finding indicates that increasing κ caused a greater increase in γ as compared to G. According to the constitutive equation for couple stress (Eq. 2), larger γ would tend to increase the couple stress. As fiber deformations transitioned from bending to stretching, it is possible that the increased γ had a greater effect on the couple stress than the decreased rotations. This reasoning is supported by the dimensionless variables Γ and Λ, which quantify the ratio of local moments and forces. As shown in Figs. 9–10, increasing κ caused Γ and Λ to increase, which indicates that the ratio of local moments and forces also increased. Therefore, greater κ causes an increase in couple stress (moment per area) that exceeds the increase of stress (force per area) in the network.

Effects of length scale occur at small size scales, in this case in cylinders having radii of tens of fiber lengths as shown in Fig. 6. It is important to consider that at these small length scales, heterogeneity due to the random fibrous structure becomes apparent. We have previously quantified heterogeneity in modulus by using contracting particles that mimicked the contraction of a cell (Proestaki et al., 2019). The data showed that for particles of diameter approximately 10 times the average fiber length, modulus varied by a factor of 1.4 at different positions within the same fiber network. In comparison, the results in bending (Fig. 6) show that for a cylinder radius $R/l_f = 10$, the relative stiffness in bending Ω_b is ≈ 3, which is larger than the effects of heterogeneity. In a different study, the typical length scale for a heterogeneously deforming group of fibers was observed to be $\approx 2.2l_f$ (Burkel et al., 2018). It may be that on this length scale, heterogeneity in stiffness would dominate effect of length scale on stiffness. But because an apparent increase in stiffness is observed for cylinders having radii up to 20 fiber lengths (Fig. 6), there exists a regime in which the length scale is large enough that the mechanics are not dominated by heterogeneity but small enough that effects of length scale are present.

The fact that fibrous materials depend on length scale may be useful in improving continuum models for these materials. The recent continuum models for fibrous materials (Wang et al., 2014; Rosakis et al., 2015; Xu & Safran, 2015; Steinwachs et al., 2016; Ban et al., 2019) have focused on behaviors such as strain stiffening and compression softening. These are nonlinear phenomena caused by alignment of fibers in tension and buckling of fibers in compression. The length-scale effects studied here differ from nonlinearity in that they occur at small strains. Models for the mechanics of fibrous materials at size scales of tens of fibers could therefore be improved by incorporating length-scale effects. The resulting combination of nonlinearity and length-scale dependence could lead to new predictions for the mechanics of fibrous materials.

Acknowledgments

We thank R. Lakes for useful discussions. We thank B. Burkel for providing the image of the collagen gel. This work was funded by National Science Foundation grant number CMMI-1749400.

Competing Interests Statement

Declarations of interest: none.

References

Aghvami, M., Billiar, K. L., & Sander, E. A. (2016). Fiber network models predict enhanced cell mechanosensing on fibrous gels. *J Biomech Eng–T ASME*, *138*(10), 101006.

Arevalo, R. C., Kumar, P., Urbach, J. S., & Blair, D. L. (2015). Stress heterogeneities in sheared type-I collagen networks revealed by boundary stress microscopy. *Plos One*, *10*(3), e0118021.

Ban, E., Wang, H., Franklin, J. M., Liphardt, J. T., Janmey, P. A., & Shenoy, V. B. (2019). Strong triaxial coupling and anomalous Poisson effect in collagen networks. *P Natl Acad Sci USA*, *116*(14), 6790–6799.

Berkache, K., Deogekar, S., Goda, I., Picu, R. C., & Ganghoffer, J.-F. (2019a). Homogenized elastic response of random fiber networks based on strain gradient continuum models. *Math Mech Solids*.

Berkache, K., Deogekar, S., Goda, I., Picu, R. C., & Ganghoffer, J.-F. (2019b). Identification of equivalent couple-stress continuum models for planar random fibrous media. *Continuum Mech Therm*, *31*(4), 1035–1050.

Broedersz, C. P., Mao, X., Lubensky, T. C., & MacKintosh, F. C. (2011). Criticality and isostaticity in fibre networks. *Nat Phys*, *7*(12), 983–988.

Burkel, B. & Notbohm, J. (2017). Mechanical response of collagen networks to nonuniform microscale loads. *Soft Matter*, *13*(34), 5749–5758.

Burkel, B., Proestaki, M., Tyznik, S., & Notbohm, J. (2018). Heterogeneity and nonaffinity of cell-induced matrix displacements. *Phys Rev E*, *98*(5), 052410.

Conti, E. & MacKintosh, F. C. (2009). Cross-linked networks of stiff filaments exhibit negative normal stress. *Phys Rev Lett*, *102*(8), 088102.

Eringen, A. C. (1968). Theory of micropolar elasticity. In H. Liebowitz (Ed.), *Fracture, an advanced treatise* chapter 7, (pp. 621–729). Academic Press.

Gauthier, R. & Jahsman, W. (1975). A quest for micropolar elastic constants. *J Appl Mech*, *42*(2), 369–374.

Grekas, G., Proestaki, M., Rosakis, P., Notbohm, J., Makridakis, C., & Ravichandran, G. (2019). Cells exploit a phase transition to establish interconnections in fibrous extracellular matrices. *arXiv preprint arXiv:1905.11246*.

Grimmer, P. & Notbohm, J. (2018). Displacement propagation in fibrous networks due to local contraction. *J Biomech Eng-T ASME*, *140*(4), 041011.

Hatami-Marbini, H. & Picu, R. C. (2008). Scaling of nonaffine deformation in random semiflexible fiber networks. *Phys Rev E*, *77*(6), 062103.

Head, D., Levine, A., & MacKintosh, F. (2003). Distinct regimes of elastic response and deformation modes of cross-linked cytoskeletal and semiflexible polymer networks. *Phys Rev E*, *68*(6), 061907.

Heussinger, C. & Frey, E. (2007). Force distributions and force chains in random stiff fiber networks. *Eur Phy J E*, *24*(1), 47–53.

Humphries, D., Grogan, J., & Gaffney, E. (2017). Mechanical cell–cell communication in fibrous networks: the importance of network geometry. *Bull Math Biol*, *79*(3), 498–524.

Islam, M. & Picu, R. C. (2018). Effect of network architecture on the mechanical behavior of random fiber networks. *J Appl Mech—T ASME*, *85*(8), 081011.

Jones, C. A., Cibula, M., Feng, J., Krnacik, E. A., McIntyre, D. H., Levine, H., & Sun, B. (2015). Micromechanics of cellularized biopolymer networks. *P Natl Acad Sci USA*, *112*(37), E5117–E5122.

Kim, O. V., Liang, X., Litvinov, R. I., Weisel, J. W., Alber, M. S., & Purohit, P. K. (2016). Foam-like compression behavior of fibrin networks. *Biomech Model Mechanobiol*, *15*(1), 213–228.

Kim, O. V., Litvinov, R. I., Weisel, J. W., & Alber, M. S. (2014). Structural basis for the nonlinear mechanics of fibrin networks under compression. *Biomaterials*, *35*(25), 6739–6749.

Korff, T. & Augustin, H. G. (1999). Tensional forces in fibrillar extracellular matrices control directional capillary sprouting. *J Cell Sci*, *112*(19), 3249–3258.

Kotlarchyk, M. A., Shreim, S. G., Alvarez-Elizondo, M. B., Estrada, L. C., Singh, R., Valdevit, L., Kniazeva, E., Gratton, E., Putnam, A. J., & Botvinick, E. L. (2011). Concentration independent modulation of local micromechanics in a fibrin gel. *Plos One*, *6*(5).

Kulesh, M. A., Matveenko, V. P., & Shardakov, I. N. (2001). Exact analytical solution of the Kirsch problem within the framework of the Cosserat continuum and pseudocontinuum. *J Appl Mech Tech Phy*, *42*(4), 687–695.

Lakes, R. (2016). Physical meaning of elastic constants in Cosserat, void, and microstretch elasticity. *J Mech Mater Struct*, *11*(3), 217–229.

Li, Y.-D. & Lee, K. Y. (2009). Fracture analysis in micropolar elasticity: mode-I crack. *Int J Fracture*, *156*(2), 179–184.

Liang, X., Chernysh, I., Purohit, P. K., & Weisel, J. W. (2017). Phase transitions during compression and decompression of clots from platelet-poor plasma, platelet-rich plasma and whole blood. *Acta Biomater*, *60*, 275–290.

Licup, A. J., Münster, S., Sharma, A., Sheinman, M., Jawerth, L. M., Fabry, B., Weitz, D. A., & MacKintosh, F. C. (2015). Stress controls the mechanics of collagen networks. *P Natl Acad Sci USA*, *112*(31), 9573–9578.

Licup, A. J., Sharma, A., & MacKintosh, F. C. (2016). Elastic regimes of subisostatic athermal fiber networks. *Phys Rev E*, *93*(1), 012407.

Lindström, S. B., Kulachenko, A., Jawerth, L. M., & Vader, D. A. (2013). Finite-strain, finite-size mechanics of rigidly cross-linked biopolymer networks. *Soft Matter*, *9*(30), 7302–7313.

Lindström, S. B., Vader, D. A., Kulachenko, A., & Weitz, D. A. (2010). Biopolymer network geometries: characterization, regeneration, and elastic properties. *Phys Rev E*, *82*(5), 051905.

Münster, S., Jawerth, L. M., Leslie, B. A., Weitz, J. I., Fabry, B., & Weitz, D. A. (2013). Strain history dependence of the nonlinear stress response of fibrin and collagen networks. *P Natl Acad Sci USA*, *110*(30), 12197–12202.

Notbohm, J., Lesman, A., Rosakis, P., Tirrell, D. A., & Ravichandran, G. (2015). Microbuckling of fibrin provides a mechanism for cell mechanosensing. *J R Soc Interface*, *12*(108), 20150320.

Onck, P., Koeman, T., Van Dillen, T., & Van der Giessen, E. (2005). Alternative explanation of stiffening in cross-linked semiflexible networks. *Phys Rev Lett*, *95*(17), 178102.

Proestaki, M., Ogren, A., Burkel, B., & Notbohm, J. (2019). Modulus of fibrous collagen at the length scale of a cell. *Exp Mech*, 1–12.

Reda, H., Berkache, K., Ganghoffer, J., & Lakiss, H. (2018). Dynamical properties of random fibrous networks based on generalized continuum mechanics. *Wave Random Complex*, 1–27.

Reddy, G. K. & Venkatasubramanian, N. (1978). On the flexural rigidity of a micropolar elastic circular cylinder. *J Appl Mech*, *45*(2), 429–431.

Rens, R., Vahabi, M., Licup, A., MacKintosh, F., & Sharma, A. (2016). Nonlinear mechanics of athermal branched biopolymer networks. *J Phys Chem B*, *120*(26), 5831–5841.

Roeder, B. A., Kokini, K., & Voytik-Harbin, S. L. (2009). Fibril microstructure affects strain transmission within collagen extracellular matrices. *J Biomech Eng–T ASME*, *131*(3), 031004.

Rosakis, P., Notbohm, J., & Ravichandran, G. (2015). A model for compression-weakening materials and the elastic fields due to contractile cells. *J Mech Phys Solids*, *85*, 18–32.

Rudnicki, M. S., Cirka, H. A., Aghvami, M., Sander, E. A., Wen, Q., & Billiar, K. L. (2013). Nonlinear strain stiffening is not sufficient to explain how far cells can feel on fibrous protein gels. *Biophys J*, *105*(1), 11–20.

Rueger, Z. & Lakes, R. S. (2016a). Cosserat elasticity of negative Poisson's ratio foam: experiment. *Smart Mater Struct*, *25*(5), 054004.

Rueger, Z. & Lakes, R. S. (2016b). Experimental Cosserat elasticity in open-cell polymer foam. *Philos Mag*, *96*(2), 93–111.

Sawhney, R. K. & Howard, J. (2002). Slow local movements of collagen fibers by fibroblasts drive the rapid global self-organization of collagen gels. *J Cell Biol*, *157*(6), 1083–1092.

Shahsavari, A. & Picu, R. C. (2013). Size effect on mechanical behavior of random fiber networks. *Int J Solids Struct*, *50*(20), 3332–3338.

Sharma, A., Licup, A., Jansen, K., Rens, R., Sheinman, M., Koenderink, G., & MacKintosh, F. (2016). Strain-controlled criticality governs the nonlinear mechanics of fibre networks. *Nat Phys*, *12*(6), 584.

Shayegan, M. & Forde, N. R. (2013). Microrheological characterization of collagen systems: from molecular solutions to fibrillar gels. *Plos One*, *8*(8), e70590.

Sopher, R. S., Tokash, H., Natan, S., Sharabi, M., Shelah, O., Tchaicheeyan, O., & Lesman, A. (2018). Nonlinear elasticity of the ECM fibers facilitates efficient intercellular communication. *Biophys J*, *115*(7), 1357–1370.

Stein, A. M., Vader, D. A., Weitz, D. A., & Sander, L. M. (2011). The micromechanics of three-dimensional collagen-I gels. *Complexity*, *16*(4), 22–28.

Steinwachs, J., Metzner, C., Skodzek, K., Lang, N., Thievessen, I., Mark, C., Münster, S., Aifantis, K. E., & Fabry, B. (2016). Three-dimensional force microscopy of cells in biopolymer networks. *Nat Meth*, *13*(2), 171.

Stopak, D. & Harris, A. K. (1982). Connective tissue morphogenesis by fibroblast traction: I. Tissue culture observations. *Dev Biol*, *90*(2), 383–398.

Vader, D., Kabla, A., Weitz, D., & Mahadevan, L. (2009). Strain-induced alignment in collagen gels. *Plos One*, *4*(6), e5902.

Vahabi, M., Sharma, A., Licup, A. J., van Oosten, A. S., Galie, P. A., Janmey, P. A., & MacKintosh, F. C. (2016). Elasticity of fibrous networks under uniaxial prestress. *Soft Matter*, *12*(22), 5050–5060.

van Oosten, A. S., Vahabi, M., Licup, A. J., Sharma, A., Galie, P. A., MacKintosh, F. C., & Janmey, P. A. (2016). Uncoupling shear and uniaxial elastic moduli of semiflexible biopolymer networks: compression-softening and stretch-stiffening. *Sci Rep*, *6*, 19270.

Velegol, D. & Lanni, F. (2001). Cell traction forces on soft biomaterials. I. Microrheology of type I collagen gels. *Biophys J*, *81*(3), 1786–1792.

Wang, H., Abhilash, A., Chen, C. S., Wells, R. G., & Shenoy, V. B. (2014). Long-range force transmission in fibrous matrices enabled by tension-driven alignment of fibers. *Biophys J*, *107*(11), 2592–2603.

Wen, Q., Basu, A., Winer, J. P., Yodh, A., & Janmey, P. A. (2007). Local and global deformations in a strain-stiffening fibrin gel. *New J Phys*, *9*(11), 428.

Wilhelm, J. & Frey, E. (2003). Elasticity of stiff polymer networks. *Phys Rev Lett*, *91*(10), 108103.

Winer, J. P., Oake, S., & Janmey, P. A. (2009). Non-linear elasticity of extracellular matrices enables contractile cells to communicate local position and orientation. *Plos One*, *4*(7), e6382.

Xu, X. & Safran, S. A. (2015). Nonlinearities of biopolymer gels increase the range of force transmission. *Phys Rev E*, *92*(3), 032728.

Yang, J. & Lakes, R. (1981). Transient study of couple stress effects in compact bone: torsion. *J Biomech Eng—T ASME*, *103*(4), 275–279.

Yang, J. & Lakes, R. S. (1982). Experimental study of micropolar and couple stress elasticity in compact bone in bending. *J Biomech*, *15*(2), 91–98.